



Multistep nucleation compatible with a single energy barrier: catching the non-classical culprit

A. Lauer, M. Durán-Olivencia, A. Fernandez-Martinez, A. van Driessche

► To cite this version:

A. Lauer, M. Durán-Olivencia, A. Fernandez-Martinez, A. van Driessche. Multistep nucleation compatible with a single energy barrier: catching the non-classical culprit. Faraday Discussions, 2022, 235, pp.95-108. 10.1039/D1FD00092F . hal-03872264

HAL Id: hal-03872264

<https://hal.science/hal-03872264>

Submitted on 25 Nov 2022

HAL is a multi-disciplinary open access archive for the deposit and dissemination of scientific research documents, whether they are published or not. The documents may come from teaching and research institutions in France or abroad, or from public or private research centers.

L'archive ouverte pluridisciplinaire **HAL**, est destinée au dépôt et à la diffusion de documents scientifiques de niveau recherche, publiés ou non, émanant des établissements d'enseignement et de recherche français ou étrangers, des laboratoires publics ou privés.

Nucleation precursors compatible with a single energy barrier: catching the non-classical culprit

A.R. Lauer¹, M.A. Durán-Olivencia^{2,3,*}, A. Fernandez-Martinez¹, A.E.S. Van Driessche^{1,4*}

- 1 Université Grenoble Alpes, Université Savoie Mont Blanc, CNRS, IRD, IFSTTAR, ISTerre, Grenoble, France.
- 2 Departamento de Telemática y Computación, Universidad Pontificia de Comillas, Madrid, Spain.
- 3 Department of Chemical Engineering, Imperial College London, London, UK.
- 4 Instituto Andaluz de Ciencias de la Tierra, IACT, CSIC – University of Granada, Granada, Spain.

*Correspondence to: madolivencia@icai.comillas.edu, alexander.vd@csic.es

Abstract

In this work we link experimental results of SrSO_4 precipitation with a mesoscopic nucleation model (MeNT) to stride towards a cohesive view of the nucleation process that integrates both classical and non-classical views. When SrCl_2 and Na_2SO_4 are co-titrated at slow dosing rates, time-resolved turbidity, conductivity and ion-specific data reveal that the initial stage of the nucleation process is driven by neutral species, i.e. ion-pairs or larger, akin to the prenucleation cluster model. However, when co-titrations are conducted at higher rates, the onset of nucleation is dominated by the consumption of free ions, akin to the classical model of nucleation (CNT). The occurrence of both mechanisms for the same system is explained by a toy model that includes both the thermodynamics (consisting of a single energy barrier) and kinetics of cluster formation formally obtained from MeNT. This gives rise to an effective barrier exhibiting a local intermediate minimum, which does not originate from a minimum in the thermodynamic free energy. Rather, it is associated with an increased probability of observing a specific class (in terms of size/density) of precursor clusters due to their slower kinetics. At high supersaturations this minimum in the kinetics of cluster formation becomes less pronounced and the effective barrier is also significantly lowered. Consequently, the probability of observing an intermediate state is blurred and we recover a nucleation pathway more closely following the one envisaged by the classical model. Thus, our model is capable of capturing both single and multistep nucleation mechanisms observed experimentally considering only a single energy barrier.

1. Introduction

Nucleation is an activated process in which a system overcomes a free energy barrier during the first-order phase transition from a metastable to a stable phase. In the particular case of crystallization from solution, it is commonly accepted that the nucleation process starts by random aggregation of ions/species in solution, which form clusters that eventually may evolve into a crystal. When accounting for the contributions of bulk (favorable) and surface (unfavorable) interactions as the randomly formed aggregates grow in size, the overall free energy of a nucleating system first increases, thus posing a barrier. Consequently, many of the initially formed clusters will quickly re-dissolve and only those that, as a result of statistical fluctuations, reach a certain critical size (where they become an actual nucleus), at which the gain in volume free energy equals the costs of surface free energy (maximum in ΔG). Any further addition of ions/species will lead to a decrease in overall energy of the nucleus, which will continue to grow to a mature crystal. According to classical nucleation theory (CNT)^{e.g. 1}, the formation of a nucleus is a one-step process that produces a microscopic particle with the same characteristics (e.g. order, density, composition, etc.) as a fully-grown macroscopic crystal. In CNT, this transition from dissolved ions/species to crystalline entities is associated with a single energy barrier (black curve, Fig. 1).

However, experimental results gathered during the last decades have challenged this classical picture by revealing that the route from a supersaturated solution to a solid (crystalline) material can involve multiple steps in which distinct precursors and/or intermediate phases occur and interconvert across different length and time scales^{e.g.2,3}. It is generally assumed that such a multi-step (or so-called non-classical) pathway also implies a multi-barrier energetic landscape for nucleation^{e.g. 4-6} (pink curve, Fig. 1). For example, some of the precursors/intermediates correspond to local free energy minima separated by individual barriers that need to be overcome for the system to transform (note that each transformation step can involve a new nucleation event, either in the condensed phase -structural reorganization- or in solution after re-dissolution). Nonetheless, recent theoretical considerations within the context of the Mesoscopic Nucleation Theory (MeNT)⁵ postulate that energy minima are not a prerequisite for multi-step nucleation to occur, since precursor species could potentially emerge due to the competition between thermodynamics and kinetics during cluster formation on a continuous uphill energy profile^{8,9} (grey curve, Fig. 1).

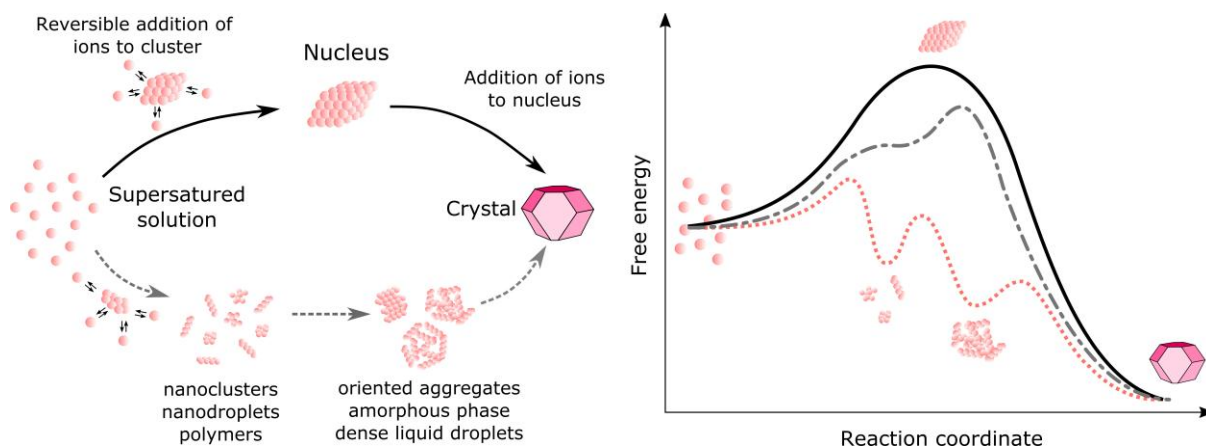


Figure 1. Schematic representation of one- and multi-step mechanisms for the formation of crystals from supersaturated solutions and their associated energy barriers: a single barrier representative for classical nucleation (black curve), a multi-step barrier model proposed for non-classical nucleation (dotted pink curve) and a multislope single barrier considered by MeNT (grey curve).

In this work we attempt to link experimental results of SrSO_4 precipitation with MeNT modeling to stride towards a cohesive view of the nucleation process. When SrCl_2 and Na_2SO_4 are co-titrated at slow dosing rates, nucleation occurs at relatively low supersaturations and time-resolved turbidity, conductivity and ion-specific data reveal that the initial phase separation is controlled by neutral species, i.e. ion-pairs or larger, akin to the pre-nucleation pathway¹⁰. When co-titrations are conducted at higher rates, nucleation occurs at considerably higher supersaturations and the data obtained from the different probes show that the initially nucleating phase is formed mainly through the consumption of free ions, akin to the CNT model. The occurrence of both nucleation mechanisms for the same system is also observed when using a toy model to describe the nucleation pathway, consisting of a single energy barrier and kinetics of cluster formation inspired by the ones formally obtained from MeNT. The potential implications of these preliminary findings and future endeavours are discussed.

2. The MeNT-based toy model

The classical nucleation theory (CNT) presents a series of inherent problems, such as the lack of consistency when expressing measurable quantities, such as the nucleation rate, as a function of one order parameter, e.g. the cluster molecular size N or the cluster radius R .^{1,11,12} In addition, CNT entails other constraints that further limit its range of applicability. It assumes a spherically symmetric nucleation cluster, with an associated work of formation determined by the equilibrium thermodynamic potential (free energy in the case of closed

systems, or Landau's potential in the case of open systems). Also, it imposes a very naïve nucleation pathway that fixes the structural properties of the clusters to be the same as the ones of the final stable bulk phase. This nucleation pathway can be represented as a straight line in the parameter space, connecting two points: zero and infinity. Nevertheless, it is reasonable to expect that clusters are not only characterised by their size, but by several other features (e.g. density/order). Thus, the assumption of clusters growing or shrinking along the cluster-size (R or N) axis with all their other properties being exactly the same as the macroscopic phase is in many cases an oversimplification of reality.

Indeed, the constraints of the CNT model come at a great cost. For example, it cannot account for the rich family of clusters that have been observed experimentally during the nucleation process of a variety of systems^{e.g. 2,3,10}. Of the main CNT constraints we have just pinpointed, the spherical symmetry and the local-equilibrium approximation do not affect the internal properties of nucleation clusters. These two assumptions are usually invoked to facilitate the mathematical expressions involved, and allow the formulation of an analytical theory in terms of manageable equations. As for the remaining constraint, the imposed nucleation pathway cancels out all clusters that are not perfect microscopic replicas of the final phase. For instance, according to CNT, if the final stable phase is a crystal then clusters must have the very same structure as the equilibrium configuration.

To overcome these inherent limitations of CNT, the description of the nucleation process used in this work relies upon a fluctuating-hydrodynamical picture of out-of-equilibrium systems, also known as mesoscopic nucleation theory (MeNT).⁷ MeNT starts from an atomistic description of out-of-equilibrium fluids, and finally recovers CNT-like expressions.^{11,13,14} To reduce the number of independent variables of the MeNT theory and obtain an explicit solution of fundamental quantities, such as the nucleation rate or the cluster distribution function, a general framework for nucleation (GFN)⁸ has been derived within the context of MeNT establishing the nucleation pathway as the core of the process. This led to a single-variable theory to describe nucleation. Thus, if we have a model for the nucleation pathway GFN will provide us with an exact expression of the cluster distribution, which can then be contrasted against experimental observations.

The key components of the nucleation model used in this work are the following:

- I. A parametric description of the density fluctuations (clusters), $\rho(\mathbf{r};t)$, in terms of measurable properties, such as cluster radius, inner density, order, etc. In order to get

tractable analytical equations, clusters are assumed to be spherically symmetric, so that $\rho(\mathbf{r}; t) = \rho(r; t)$. The parametric description of clusters is then accomplished by introducing a parameterisation in terms of those variables:

$$\rho(r; t) = \rho(r; x_1(t), x_2(t), \dots, x_N(t)) \quad (1)$$

where $x_1(t), x_2(t), \dots, x_N(t)$ are the so-called order parameters (or reaction coordinates.) CNT is recovered by setting $x_1(t) = R(t)$, with R being the cluster radius, and maintaining all the other properties constant and equal to the values of the final equilibrium phase. A more general theory than CNT is reached by setting: $\rho(r; t) = \rho(x_1 = R(t), x_2 = \rho_0(t))$, with ρ_0 being the average inner density of the cluster, assumed constant inside the cluster, now free to change unlike in CNT. For the sake of brevity, we will drop the time-dependency of the order parameters, by simply referring to them as x_1, x_2, \dots, x_N , bearing in mind the underlying dependency. In this study, we will consider a two-variable description of clusters, although more order parameters could be added if needed. However, it has been shown that a two-variable description is good enough to capture the most important aspects of nonclassical nucleation pathways whilst keeping the theory analytically tractable.^{8, 13}

- II. A model for the free energy functional, $\Omega[\rho] = \Omega(x_1, x_2, \dots, x_N)$, which determines the equilibrium states of the system. For this we will use a standard fluid equation of state, based on the thermodynamic perturbation theory.^{15, 16} Once we have a model for the free energy of the system, we will be able to build the nucleation barrier by differencing the energy in presence of a cluster, $\Omega[\rho]$, and the energy of the system in the absence of any cluster, $\Omega[\rho_\infty]$, where $\rho_\infty = \lim_{r \rightarrow \infty} \rho(r; t)$, which refers to the average density of the in metastable phase. This has been shown to yield a prototypical volume-vs-surface barrier.¹³
- III. A nucleation pathway, Γ , which represents a trajectory in the parameter space (i.e., the space where the coordinate axes are the order-parameter variables mentioned above). As any trajectory in a geometric space, the pathway can be rewritten in terms of the natural arc-length parameter, s , or by any other variable which is one-to-one related to s . The average inner density of the cluster, ρ_0 , is in one-to-one relationship with s , as was shown elsewhere.^{7, 8} This is quite convenient given that ρ_0 is experimentally accessible, unlike the arc-length of the nucleation pathway. Hence, from hereon we will not differentiate between s and ρ_0 .

Now, based on the nucleation trajectory Γ where the clusters will be fluctuating over, and the cluster-density parameterisation, a steady-state and equilibrium cluster distributions (i.e. the probability density functions to find a cluster at any point of the nucleation pathway, with the properties determined by the value of s) can be derived:⁸

$$P_{st}(s) = A_{st} \sqrt{g(s)} e^{-\beta\Omega(s)} \int_s^{s_+} dz \sqrt{g(z)} e^{\beta\Omega(z)} \quad (2)$$

$$P_{eq}(s) = A_{eq} g^{\frac{1}{2}}(s) e^{-\beta\Omega(s)} = A_{eq} \exp\left(-\beta\Omega(s) + \frac{1}{2} \log g(s)\right) \quad (3)$$

where A_{st} and A_{eq} are normalisation constants, $g(s)$ is the so-called metric function which recovers the monomer attachment rate in the case of a single parameter $x_1 = R$, $\beta = 1/k_B T$ is the reciprocal temperature, and $s_+ = (1 + \epsilon)s_*$ is a boundary point in the vicinity of the critical cluster s_* separating the nucleation and growth stages, with $\epsilon < 1$. The steady-state and equilibrium distributions of the clusters are nearly identical within the pre-critical region of the parameter space, as was shown recently.⁸ For this reason, we focus our attention on the equilibrium distribution, as it is more straightforward and contains all the elements necessary to study a nucleation process.

The metric function $g(s)$ represents the kinetics of cluster formation, given that it recovers the monomer attachment rate from CNT when a single order-parameter description of the cluster is adopted.¹¹ This is worth mentioning because, if we have a careful look at the equilibrium cluster distribution (eq. 3), the kinetics can be embedded in an effective energy barrier that allow us to rewrite P_{eq} as a standard Arrhenius-like equation:

$$P_{eq}(s) = A_{eq} \exp\left(-\beta\Omega_{eff}(s)\right) \quad (4)$$

with

$$\beta\Omega_{eff}(s) = \beta\Omega(s) - \frac{1}{2} \log g(s) \quad (5)$$

This is the essential part of this model, because it allows studying the properties of the cluster distribution by merely observing the behaviour of the effective energy barrier $\beta\Omega_{eff}(s)$. The outcome of this approach is described in detail in the result section.

3. Materials and methods

3.1. Co-titration experiments

Stock solutions of SrCl_2 and Na_2SO_4 were prepared by dissolving $\text{SrCl}_2 \cdot 6\text{H}_2\text{O}$ (Arcos organics, 99% extra pure) and Na_2SO_4 (Carl Roth, $\geq 99\%$ pure) in deionized water. Using both stock solutions, equimolar potentiometric co-titrations were conducted using a Metrohm 905 Titrando equipped with two 800 Dosino devices both controlling a 20 mL dosing unit which has a minimum dosing speed of 0.015 ml/min. The titrants were added to 50 mL of deionized water in a 20-90 mL Titration Vessel purchased from Metrohm. A 20x6 mm Teflon-coated stir bar at 500 rpm agitated the reaction. The reaction was monitored simultaneously for transmittance (Metrohm optrode - part 6.115.000), conductivity (Metrohm 5-ring conductivity measuring cell $c = 0.7 \text{ cm}^{-1}$ with Pt1000 - part 6.0915.100), and cation concentration (Ion Selective Electrode that consisted of two half-cells: a Mettler-Toledo DX337-Ba membrane with a Metrohm LL ISE reference electrode - part 6.0750.100).

ISE calibration was conducted to convert voltage readouts to actual free ion concentrations. These calibrations were carried out in two steps by titrating SrCl_2 (100 mM at 0.5 ml/min) and NaCl (200 mM at 0.5 ml/min) into deionized water. This allowed for the accounting of the effect of both cations on the measured potential. From each calibration curve, the Nernstian equation was fitted for the parameters U_0 and p (the sign of p has been changed from standard representation for clarity):

$$U = U_0 + p \cdot \log(c + c_0) \quad (6)$$

with c_0 assumed to be negligible. The fitting procedure first found the slope of $\log(c_{\text{dosed}})$ vs. U to fit for the parameter p . Then, the equation can be rearranged to find:

$$e^{U/p} = c \cdot e^{U_0/p} \quad (7)$$

and treating $e^{-U_0/p}$ as a constant K , we obtain an easy expression for treating the data where:

$$c_{\text{measured}} = e^{U/p} / K \quad (8)$$

K was determined by plotting the concentration of dosed ions against the function $e^{U/p}$ using the p parameter defined in the first step. For each titration, this calibration procedure was conducted two times with strontium chloride and one time with sodium chloride. With a new ISE, the s parameter was found to be quite consistent (standard deviation below 3%), so to determine the $1/K$ parameter for sodium, the average p for the strontium calibrations was

used. Then the two $1/K$ parameters were summed, and applied to the experimental data alongside the s parameter obtained from the strontium calibration.

Different dosing rates were used to vary the saturation rate across several orders of magnitude (Table 1). At the point of nucleation, we know the concentration of ions that has been dosed into the solution and from this the critical saturation index, SI_{crit} , relative to the solid phase (i.e. celestite) was calculated using Phreeqc¹⁷ and the BRGM Thermoddem geochemical database.¹⁸ As expected, SI_{crit} increased with increasing dosing rates (Table 1).

Table 1. Dosing rates and the critical supersaturation index, SI_{crit} , at which nucleation is first detected. The error represents the standard deviation from three replicate experiments.

Dosing rate (mol.min ⁻¹)	SI_{crit}	error
0.002	1.15	0.08
0.010	1.33	0.04
0.100	1.63	0.01
0.500	1.91	0.01
1.000	2.02	0.02

3.2. Nucleation point determination

During co-titration experiments, three probes, i.e. optrode, ion selective probe and conductivity probe, were used to monitor in situ the nucleation process. From these time-resolved data the onset of phase transition was determined by an automated analysis routine based on the changes in the behavior of the first derivative, i.e. the time point of nucleation was defined when the first derivative reached 5% of its minimum value. For optical transmittance, this was the point at which the derivative became non-zero. Both the conductivity and free cation concentration curves had a downward concavity that required a more complex algorithm to precisely define the time of nucleation observed by those probes. To this end, the curves were smoothed, derived, smoothed again, and then the slope before the nucleation point was fit with a line. Nucleation was defined as the point at which the first derivative deviated significantly (5%) from that fit line.

4. Results and discussion

4.1. Co-titration experiments

In order to study the evolution of the ionic environment during the precipitation of strontium sulfate, equimolar co-titrations were conducted in which equal amounts of Sr^{2+} and SO_4^{2-} were added at a steady rate into a reaction vessel containing 50 mL of deionized water and continuously stirred to assure a homogeneous mixing. These titrations were monitored for cation activity, transmittance and conductivity (Fig. 2a). The first stage of these titrations is characterized by a monotone increase of cation activity and conductivity with a steady state transmittance signal. Upon nucleation, a second stage is reached in which transmittance drops sharply, while the conductivity signal starts to flatten out and the free ion curve experiences a drop. The point at which these changes occur is defined as the onset of nucleation and was determined by an automated analysis routine based on the behavior of the first derivative.

A close examination of Fig. 2a (see insets) shows that there is an apparent difference between the nucleation times measured by the transmittance probe and those measured by the ISE and conductivity. Using the previously described method to determine the nucleation time from the different data sets it is possible to compare between the probes for experiments run with different dosing rates, from 0.002 to $1 \text{ mol} \cdot \text{min}^{-1}$. From these dosing rates and the known volume of the reaction solution volume the critical saturation index, SI_{crit} , at the nucleation time point can be calculated (Table 1).

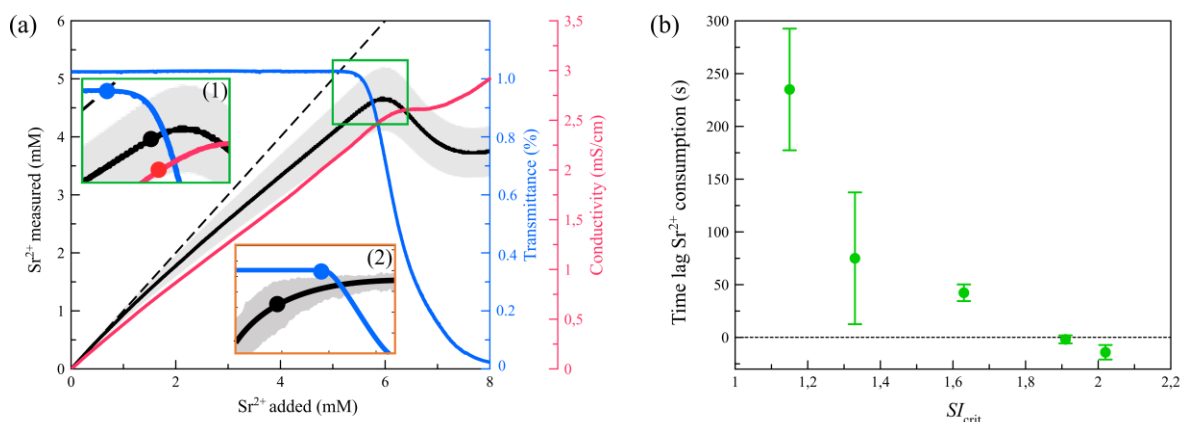


Figure 2. SrSO_4 nucleation times monitored using co-titration experiments. (a) Example of an equimolar co-titration experiment at low dosing rate showing the time evolution of Sr^{2+} concentration (black), optical transmittance of the solution (blue), and the conductivity (red). For reference, the total added strontium concentration is shown (dashed line). Inset 1 (green square) shows an enlarged view of the nucleation event, which is defined as the point where transmittance begins to decrease or when the increases in Sr^{2+} concentration and conductivity

slow. The nucleation points are indicated by large dots added to each curve. Inset 2 (orange square) shows a zoom in of the relevant area for the highest SrSO_4 dosing rate indicating that nucleation is detected first by the ISE. (b) Difference in measured nucleation time between the transmittance probe and the ISE as a function of the critical SI at which nucleation occurred. A positive difference means the optrode detected the phase transition before the ISE. Error bars represent the standard deviation of three replicate experiments.

At the three lowest dosing rates, and thus lowest SI_{crit} , the transmittance probe detected that the formation of a new phase significantly before the ISE and conductivity probe registered the consumption of free ions (Fig. 2b). Importantly, this effect is most pronounced at the lowest dosing rate – where relatively low saturations would result in the lowest possible probe lags. This observation can be explained if we consider that the first step in strontium sulfate nucleation occurs via the consumption of neutral – i.e. bound – species that are not detected by the ISE. Indeed, Fig. 2a shows that the detected free Sr^{2+} is lower than the total added strontium, confirming the presence of bound ions that can be consumed to create this effect. Consequently, the particles detected by the optrode are formed through the aggregation of neutral particles, the smallest of which could be ion pairs. It is important to note here the error margin in the calibration of the ISE, which is represented by the grey shaded area surrounding the free ion curve in the main plot of Fig. 2a. This error represents the absolute maximum and minimum that the true reading for Sr^{2+} concentration could be considering 4 calibrations and two experiments, all conducted with a new ISE membrane on the same day (the error in the inset (2) comes from a different source – the standard deviation of three replicate experiments). While a significant portion of the shaded region coincides with the unity line (where free $\text{Sr}^{2+} = \text{dosed Sr}$), it is important to note that above the low concentration regime ($\sim 2 \text{ mM Sr}$), the rate of change is less than one. In the low concentration regime, the results from this ISE are highly irreproducible and should not be considered as meaningful, and thus it is significant that the slope of the curve outside this regime indicates ion pairing or complexation even when considering the measurements least favorable to this hypothesis. Unfortunately, the inconsistency in the low concentration regime means we are unable to comment about the pairing and complexation of Sr^{2+} in this system below its saturation concentration ($\sim 0.7 \text{ mM}$ under experimental conditions).

Now, we focus on the two highest dosing rates used for the co-titrations of SrSO_4 . In these experiments, the early detection of nucleation by the transmittance probe vanishes and at the highest dosing rate (1.0 mol.min^{-1}), the detection of nucleation by transmittance even lags behind the potentiometric detection of nucleation (Fig. 2a, inset 2). An example of typical

data from an experiment at this dosing rate is shown in Fig. 1a. Hence, at high dosing rates, i.e. high supersaturations, the first stage of nucleation is mainly driven by ion consumption and not by bound species. The fact that at the highest supersaturation the transmittance probe lags behind is probably due to the very small size of the initial nuclei, which go undetected at the used wavelength (660 nm). In short, the above-discussed experimental observations reveal that as the supersaturation rate, and thus also the critical supersaturation, increases during SrSO_4 co-titrations, the preferred nucleation mechanism changes.

4.2. The effective nucleation barrier: Thermodynamics meets kinetics

In this section we present the outcome of our theoretical modelling which was driven by the equations of GFN⁸ for the cluster distribution after adopting a model nucleation pathway inspired by the one obtained from a two-variable MeNT.¹³ As we mentioned in section 2, to obtain a nucleation barrier a model for the free-energy functional of the system is required. For this, we used a fluid equation of state (EOS) to build an energy barrier, $\Delta\Omega[\rho]$, based on the Barker-Henderson perturbation theory with the reference system given by the Carnahan-Starling EOS, which has been shown to be well-suited for the description of transitions from low-density to high-density states.^{7,8,11,13,14} We used this model EOS to initially obtain the bulk densities at coexistence for a given temperature, i.e. $\rho_\infty^{(c)}$ for the low-density phase and $\rho_0^{(c)}$ for the high-density state at a given β . Once these values have been determined, we place our simulated system into a supersaturated initial metastable state by imposing a density of $\rho_\infty = S \times \rho_\infty^{(c)}$, with $S = \rho_\infty / \rho_\infty^{(c)}$. Regarding the model of the nucleation barrier, $\beta\Omega$, we consider the surface-vs-volume barrier:^{1,7,11,13}

$$\Delta\Omega(R, \rho_0) = V(R, \rho_0)\Delta\omega + S(R, \rho_0)(\rho_0 - \rho_\infty)^2\sigma \quad (9)$$

with $\Delta\omega = \omega(\rho_0) - \omega(\rho_\infty)$ being the negative increment in the system's pressure in the presence of a cluster of volume and surface, $V = \frac{4\pi}{3}R^3$ and $S = 4\pi R^2$, respectively; and σ a constant which defines the planar surface tension.

Now that we have established the bulk system at a given temperature and a given initial density, ρ_∞ , we need to introduce a nucleation pathway so that we can compute $\beta\Omega_{eff}(s)$ along such a trajectory. As mentioned above, our pathway is inspired by the one obtained from MeNT,¹³ which selects the most probable pathway by following the steepest-descent path over the energy landscape. The resulting pathway has a characteristic U-shape (Fig. 3)

and can be divided into three stages:¹¹ (i) the first part consists of large-size-low-density fluctuations (bottom branch in Fig. 3), followed (ii) by a densification at an almost constant size (between $R=1$ and $R=2$) and finally, (iii) the growth stage of the clusters (top branch in Fig. 3). Here, we assume a similar U-shaped nucleation pathway.

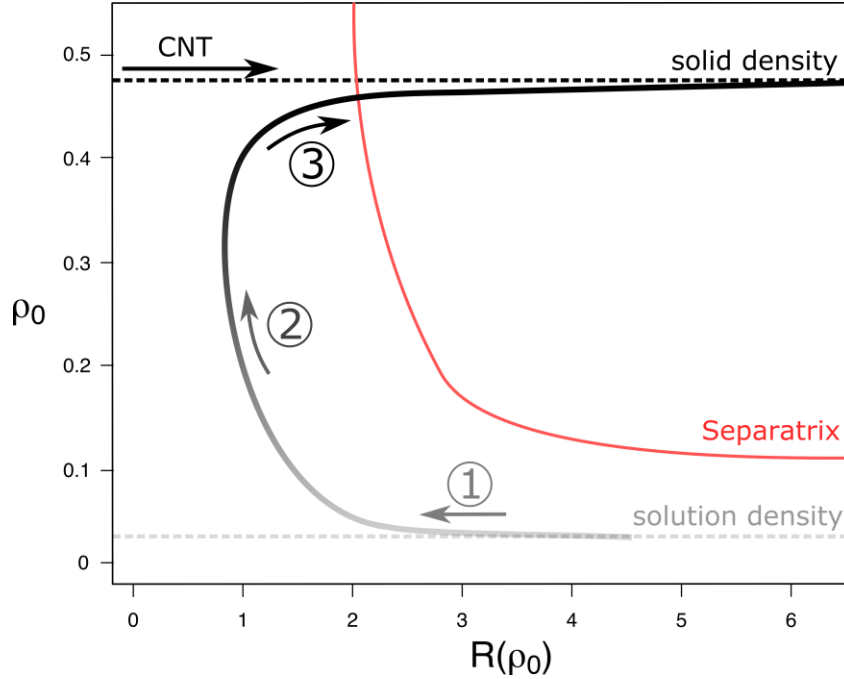


Fig 3. Model nucleation pathways predicted by MeNT and CNT. Bottom and top dashed lines represent the initial and final stable-state densities, calculated using the EOS. To achieve nucleation the separatrix must be crossed. The critical cluster for each pathway is the intersection between the pathway and the separatrix. The MeNT pathway shows three main stages:¹³ (1) contraction of the large-size-low-density fluctuations (bottom branch); (2) densification at an almost constant size (between $R=1$ and $R=2$, left branch); and, finally, (3) the growth stage of the clusters (top branch). During this final stage, the MeNT is similar to the CNT pathway, where the interior density is comparable to that of the bulk solid phase and only the size, i.e. R , changes.

Having established the nucleation pathway (Fig. 3), we now apply the equations previously discussed (section 2), and study the effects of kinetics on the pre-critical cluster distribution. Fig. 4a shows the outcome of a computation of the thermodynamic energy barrier along the natural parameter $s \sim \rho_0$ for a set of ten supersaturation values, $S \in [1.75, 3.25]$, which results in a nucleation barrier of approximately $80 k_B T$ at 1.75 and that decreases with increasing supersaturation (red arrow Fig. 4a). In Fig. 4b the computed effective energy barriers for the same set of supersaturation values, $S \in [1.75, 3.25]$, is shown. Simultaneously, Fig. 5a shows how this translates into the probabilities of observing a cluster of any given density between the values of the initial metastable and the final stable state.

Remarkably, the effective energy barrier displays a minimum at an intermediate density between the mother phase and the critical-cluster density values. This has a direct impact on the cluster probability distribution (Fig. 5a), which, as we can observe, shows an intermediate local maximum of probability in pre-critical densities. Hence, the kinetic term does not affect all pre-critical clusters in the same way, since it induces a local minimum of the effective potential at an intermediate density, ρ_m , which is related to a maximum of probability. This tells us that such intermediate clusters will be observable before nucleation happens, therefore behaving as nucleation precursors.

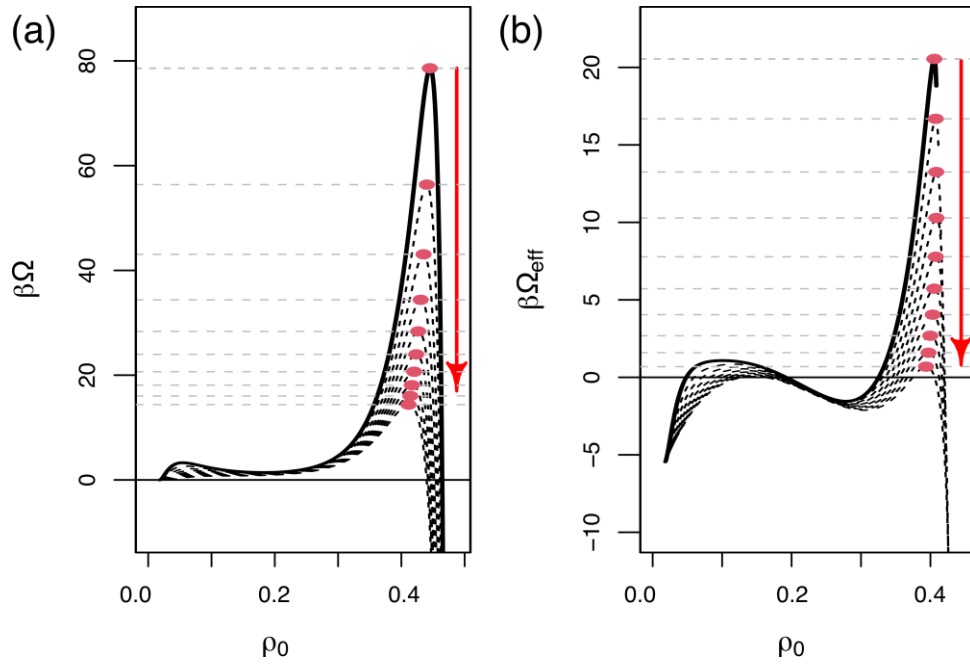


Figure 4. Energy barrier (left panel) and effective energy barrier (right panel) for a range of supersaturation values $S \in [1.75, 3.25]$. Solid black line corresponds to $S = 1.75$, while all the other supersaturation values are represented as black-dashed lines. Red circles represent the critical clusters, and grey-dashed lines are drawn as a guide to the eye to highlight the nucleation barrier for each S value. Red arrows shows the direction of increasing S values.

Importantly, the local intermediate minimum observed in Fig. 4b does not come from a minimum of the thermodynamic free energy but emerges after taking into account the kinetics of cluster formation. This indicates that apparent multi-step energy barriers can be the result of the kinetics of cluster formation, while actually involving just a single energy barrier. But, Fig. 5a shows that with increasing supersaturation the likelihood of observing pre-critical clusters over a broad range of intermediate densities grows. This gradually decreases the importance of any specific region along the density axis (say the vicinity of an intermediate density, ρ_m), since any pre-critical density becomes more and more accessible

as the supersaturation increases. Consequently, a separation between a specific class of pre-nucleation clusters and the eventual nucleation event becomes less and less evident as the supersaturation value increases. Eventually, the effective energy is so low that all possible pre-critical densities, i.e. from monomers and onward, are all likely to be observed, making it harder to differentiate any specific class of precursor clusters.

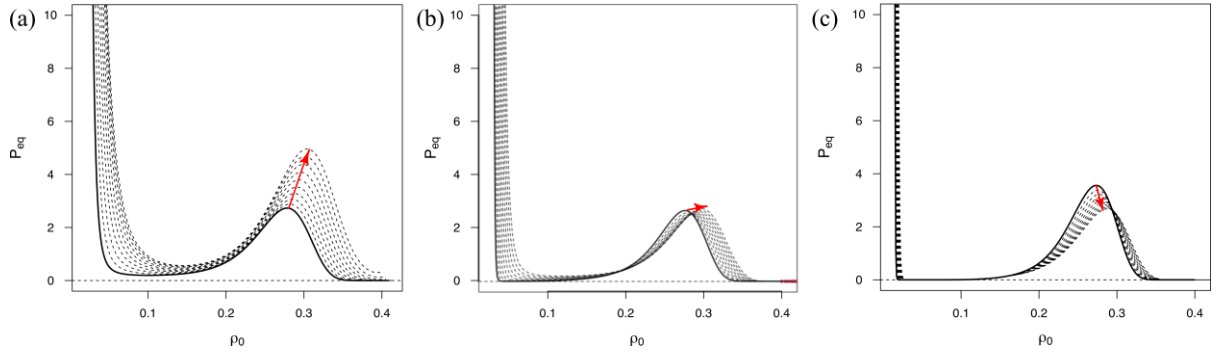


Figure 5. Equilibrium probability distributions ($P_{eq} \sim e^{-\beta\Omega_{eff}}$) of clusters associated with the supersaturation values $S \in [1.75, 3.25]$ (a), $S \in [1.01, 1.75]$ (b) and $S \in [0.75, 1.0]$ (c). Solid black line corresponds to $S = 1.75$, $S = 1.01$ and $S = 0.75$, respectively. All the other supersaturation values are represented as black-dashed lines and the red arrow indicates increasing S values.

Since a well defined population of precursor clusters appears to be more evident as the supersaturation decreases we also studied a lower interval of supersaturation values $S \in [1.01, 1.75]$, which is shown in Fig 5b. As can be observed, the results show that the emergence of precursor clusters is consistent even for very low supersaturations. Provided that the cluster-formation pathway remains unaltered for undersaturated conditions, we could in principle also study whether these intermediate densities would still be there. The results for undersaturated conditions, i.e. $S < 1$, are shown in Fig. 5c. The results of our analysis for the supersaturation range $S \in [0.7, 1.0]$ are rather remarkable: (i) precursor clusters are also present for undersaturated conditions and (II) gain importance (in terms of likelihood to be observed) as the density of the motherphase is reduced, i.e. as the system gets farther from the coexistence line.

It is worth noting that the precursor clusters described in the present model will appear in the mother phase almost instantaneously, and will persist throughout the whole nucleation process. This is because they appear as a bump of probability in the stationary cluster distribution. If anything, the time for them to be observed would be approximately the relaxation time of the cluster distribution, which is typically on the order of the diffusion time

(which is negligible in most nucleation experiments). Regarding the characteristic size and density of such clusters, they are associated with the left branch (densification stage) of the nucleation pathway depicted in Fig. 3. Hence, their inner density is approximately the same as the critical cluster of the final equilibrium phase. Taking their associated range of densities, and checking the nucleation pathway, this means that these will be considerably smaller than the critical cluster, approximately on the order of one or two molecular radii.

Thus, on a qualitative level the characteristics of the precursor clusters observed in the model are comparable to the neutral species, i.e. ion pairs or larger, detected in the SrSO_4 co-titration experiments. Moreover, the observed evolution of the system with increasing supersaturation in the model and experimental results follow the same trend, i.e. with increasing supersaturation the role of a specific (in terms of size/density) class of precursor clusters in the nucleation process becomes less pronounced. The observed trend in the model at undersaturated conditions, i.e. increasing probability distribution of precursor clusters, could not be confirmed experimentally due to the large errors associated with the ISE measurements in the low concentration (undersaturation) regime of the SrSO_4 system. Notwithstanding, prenucleation clusters at undersaturated conditions have been observed experimentally for the CaCO_3 system.¹⁰

5. Implications

Up to now, classical nucleation has been associated with a single energy barrier (black curve, Fig. 1), while non-classical (multi-step) nucleation pathways are usually linked to an energy landscape including multiple individual barriers and/or local minima (pink profile, Fig. 1). Nonetheless, the preliminary experimental and model results presented in this study point towards the fact that such a complex energy landscape is not a prerequisite to warrant multi-stage crystallization, since precursor species can also emerge due to the competition between thermodynamics and kinetics during cluster formation on a continuous uphill energy profile. Interestingly, the resulting effective energy landscape significantly changes as a function of supersaturation and reveals that more than one nucleation mechanism is attainable for one system without changing the thermodynamic barrier of the system. It is important to note that the precursor particles observed in the model do not represent a thermodynamic phase, but rather transient particles that in a specific region of the U-shaped nucleation pathway have

slower kinetics which renders them “observable”. Stated differently, this specific low kinetic region of the effective barrier corresponds with a certain size/density of precursor clusters, which disguises them as a microscopic phase with a local energy minima. It is not inconceivable to consider that such kinetically induced precursor clusters have been frequently observed in recent times due to the advent of imaging, scattering and spectroscopy tools with high spatial and time resolutions.³

As in CNT, in our model nucleation also occurs through inherent thermal fluctuations that take the system over a nucleation barrier, which is largely defined by the chemical potential and mass-transport kinetics (opposed to the surface energy of the nucleus in CNT). The effective energy landscape that arises offers a plausible explanation for our data, as well as other in situ and in silico observations of systems where precursor clusters appear to play a decisive role, including CaCO_3 ,¹⁰ CaSO_4 ,¹⁹ NaCl ,²⁰ proteins,²¹ pharmaceutical compounds,²² quantum dots²³ or metals²⁴. Future challenges to support our model concern the U-shaped nucleation pathway derived by MeNT. In particular, the initial long-wavelength low-density fluctuations, which have been observed in Monte Carlo simulations using forward-flux sampling,²⁵ but still await experimental confirmation. Also, the current mono-component system should be extended to a multicomponent system, which will be a more realistic representation of e.g. salt nucleation. Additionally, the influence of the shape of the pathway on the probability distribution of precursor clusters needs to be addressed in detail.

6. Concluding remarks

This work represents a first attempt to merge experimental evidence of nonclassical mechanisms for nucleation and state-of-the-art theoretical advances that have been put forward in recent years. The application of such recent theories to experimental evidence has been severely hampered by the complexity of theoretical formalisms (for practitioners) and by the non-ideal experimental environment (for theoreticians). This has led to a parallel, yet largely disconnected, evolution of both theory and experiments. This needs to be resolved in order for the field to keep advancing. This work argues in favour of MeNT as a holistic nucleation theory capable of inherently capturing recent nonclassical observations without relying upon ad-hoc “designed” energy landscapes. Nonetheless, MeNT needs to further evolve in order to attain the capacity of fully describing multi-component systems. This is

paramount to provide nucleation practitioners with a theoretical tool capable of predicting the outcome of a nucleation process.

Acknowledgements

A.R.L., A.F.M and A.E.S.V.D. acknowledge the French national research agency, ANR, for funding through the project CATCH, ANR-18-CE05-0035-03.

References

1. D. Kashchiev, *Nucleation: Basic Theory With Applications*, Butterworth-Heinemann, Oxford, 2000.
2. J. J. De Yoreo, P. U. P. A. Gilbert, N. A. J. M. Sommerdijk, R. L. Penn, S. Whitlam, D. Joester, H. Zhang, J. D. Rimer, A. Navrotsky, J. F. Banfield, et al., *Science* 2015, **349**, aaa6760.
3. A. E. S. Van Driessche, M. Kellermeier, L.G. Benning, and D. Gebauer. Eds. *New Perspectives on Mineral Nucleation and Growth: From Solution Precursors to Solid Materials*. Springer International Publishing, Cham, 2017.
4. P. G. Vekilov. *Cryst. Growth Des.* 2010, **10**, 5007–5019.
5. D. Gebauer, P. Raiteri, J.D. Gale and H. Colfen. *Am. J. Sci.*, 2018, **318**, 969-988.
6. J. De Yoreo. In ACS Symposium Series; Zhang, X., Ed.; American Chemical Society: Washington, DC, 2020; Vol. 1358; pp 1–17.
7. J. F. Lutsko *J. Chem. Phys.* 2012, **136**, 034509.
8. M. A. Durán-Olivencia, P. Yatsyshin, S. Kalliadasis and J. F. Lutsko. *New J. Phys.* 2018, **20**, 083019.
9. J. F. Lutsko, *Sci. Adv.* 2019, **5**, eaav7399,
10. D. Gebauer, A. Volkel and H. Colfen, *Science*, 2008, **322**, 1819–1822.
11. J. F. Lutsko and M. A. Durán-Olivencia. *J. Chem. Phys.* 2013, **138**, 244908.
12. K. Kelton and A. L. Greer , *Nucleation in Condensed Matter: Applications in Materials and Biology*, Pergamon Materials Series, 2009.
13. J. F. Lutsko and M. A. Durán-Olivencia. *J. Phys.: Condens. Matter* 2015, **27** 235101.

14. M. A. Durán-Olivencia and J. F. Lutsko. *Phys. Rev. E* 2015, **91**, 022402.
15. J. Hansen and I. McDonald, *Theory of Simple Liquids* (San Diego, CA: Academic), 1986
16. N. F. Carnahan and K. E. Starling. *J. Chem. Phys.* 1969, **51**, 635–6.
17. D.L. Parkhurst and C.A.J. Appelo, User's guide to PHREEQC - a computer program for speciation, reaction-path, 1D-transport, and inverse geochemical calculations, U.S. Geol. Survey Water Res. Invest. Rep. 1999, 99, 4259.
18. P. Blanc, A. Lassin, P. Piantone, M. Azaroual, N. Jacquemet, A. Fabbri, and E. C. Gaucher. *Appl. Geochemistry* 2012, **27**, 2107-2116.
19. T. M. Stawski, A. E. S. Van Driessche, M. Ossorio, J.D. Rodriguez-Blanco, R. Besselink and L. G. Benning. *Nat. Commun.* 2016, **7**, 11177.
20. H. Hwang, Y. C. Cho, S. Lee, Y.-H. Lee, S. Kim, Y. Kim, W. Jo, P. Duchstein, D. Zahn and G. W. Lee. *Chem. Science* 2021, **12**, 179–187.
21. A.E.S. Van Driessche, P.H.H. Bomans, R.R.M. Joosten, D. Gil-Carton, N.A.J.M. Sommerdijk and M. Sleutel. *Nature* 2018, **556**, 89- 94.
22. Y. Tsarfati, I. Biran, E. Wiedenbeck, L. Houben, H. Cölfen and B. Rybtchinski. *ACS Cent. Sci.* 2021, **7**, 900–908.
23. D. C. Gary, M. W. Terban, S. J. L. Billinge and B. M. Cossairt. *Chem. Mater.* 2015, **27**, 1432–1441.
24. J. B. K. Cao, C. T. Stoppiello, R. L. McSweeney, T. W. Chamberlain, Z. Liu, K. Suenaga, E. Besley, S. T. Skowron, A. N. Khlobystov and U. Kaiser. *Nat. Chem.* 2020, **12**, 921–928.
25. J. F. Lutsko and J. Lam. *Phys. Rev. E* 2020, **101**, 052122.